Supplementary information of article "Phases of surface-confined trivalent particles"

P. J. M. Swinkels,[1] Z. Gong,[2] S. Sacanna,[2] Eva G. Noya,[3] and Peter Schall[4]

[1] *Institute of Physics, University of Amsterdam, Amsterdam, The Netherlands*

[2] *Molecular Design Institute, Department of Chemistry, New York University, USA.*

[3] *Instituto de Química-Física Rocasolano, CSIC, Madrid, Spain.*

[4] *Institute of Physics, University of Amsterdam, Amsterdam, The Netherlands*

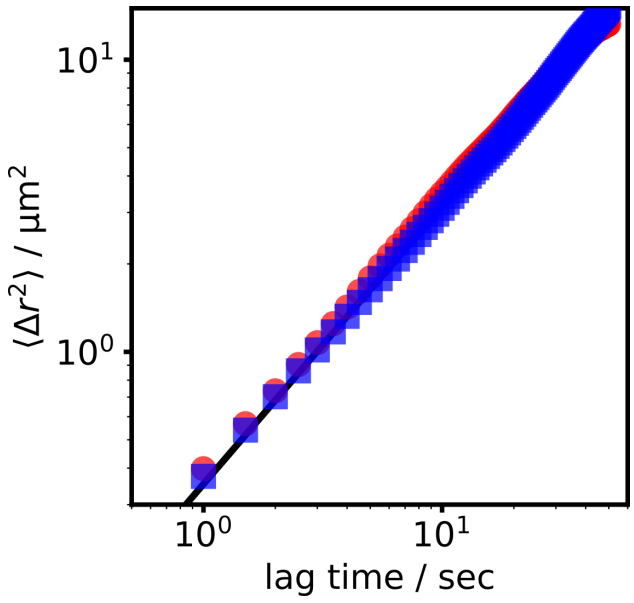

Supplementary Figure 1. **Mean square displacement (MSD) of particles bound to the surface.** Red circles indicate $\Delta T = 0.60°C$, blue squares $\Delta T = 0.05°C$. The MSD can be fitted using the equation $\langle r^2 \rangle = 4D \cdot t^n$, where D is the diffusion coefficient, t is the lag time, and n is the exponent. In an ideal system of free diffusion, $n = 1$. The black solid line is a fit of our data, yielding a diffusion coefficient $D = 0.88 \mu m^2/s$ and $n = 0.95 \pm 0.05$.

SUPPLEMENTARY NOTE 1: DIFFUSION OF PARTICLES BOUND TO THE SURFACE

To check the influence of the surface attraction on the mobility of the particles, we determined the mean square displacement of particles at the glass at $\Delta T = 0.05$ and $\Delta T = 0.60$, see Supplementary Figure 1. These temperatures correspond to the extreme cases of maximal critical Casimir attraction explored, and minimal Casimir attraction required for the particles to adsorb at the surface. Nevertheless, the mean-square displacement of the particles overlap, suggesting negligible influence of the attraction on the mobility: we observe a power-law behaviour with slope ~ 1, as expected for free diffusion, and with diffusion constant $D = 0.88 \mu m^2/s$. Furthermore, the two different attractions investigated show the same diffusion constant within error bars. Apparently, the attraction of the particles to the wall does not influence the particles' diffusion; it remains freely diffusive along the plane.

SUPPLEMENTARY NOTE 2: RADIAL DISTRIBUTION PEAKS

Figure 3b in the main text shows the radial distribution function of the honeycomb, triangular and amorphous phases. As discussed, the typical distances revealed by the radial distribution function of these three condensed phases coincide due to their shared structural motifs. The radial distribution function of the honeycomb lattice without normalization is shown in Supplementary Figure 2a, where each characteristic distance is indicated. These distances are depicted in a sketch of the honeycomb and triangular lattice in Supplementary Figure 2b. Supplementary Figure 2c highlights the small difference in internal distances of a 5-, 6-, and 7-membered ring: the two possible distances within a ring, indicated with red and blue are very similar in all three ring types.

SUPPLEMENTARY NOTE 3: PARTICLE NEIGHBOURHOOD

In the main text, we briefly discuss the short-range order of the amorphous phase and the absence of long-range order, as highlighted by the radial distribution function in Figure 3b. Here, we further examine the short-to-medium range order of the amorphous phase by studying the local ring neighbourhood in more detail. We find all particle rings in the structure and determine the probability to find an n-membered ring as neighbour to an m-

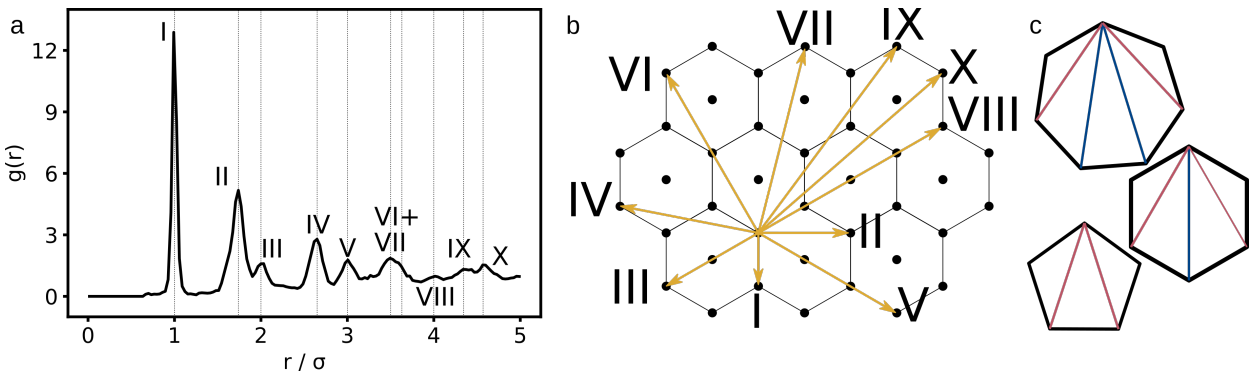

Supplementary Figure 2. **Typical distances in an open lattice.** The characteristic distances of the honeycomb lattice are labelled with Roman numerals in its radial distribution function (a). These distances are schematically denoted in a sketch of the honeycomb lattice in (b). In (c), the small difference in typical internal distances of 5-, 6-, and 7-membered rings is indicated, highlighting why the amorphous networks still show the same typical distances as a regular honeycomb lattice.

membered ring, see Supplementary Figure 3a-c. In the honeycomb phase (shown in yellow), 5-, 6-, and 7-membered rings are all most likely to have a neighbouring 6-membered ring. However, it is clear that 5-membered rings are much more likely to be next to a 7-membered ring instead of another 5-membered ring and visa versa. This is in line with the fact that neighbouring 5- and 7-membered rings experience significantly less bonding strain: a 'scar' of 5- and 7-membered rings is a typical defect seen in assemblies of trivalent, surface-confined building blocks because it is geometrically relatively stable [1]. In the amorphous case (shown in blue), the distribution is much more ambivalent: All ring sizes have nearly equal probability of being next to any other ring. This is hardly surprising considering the random packing of these many-sized rings.

A related metric is the probability of ring-triplet combinations, given in Supplementary Figure 3d: the probability of finding 3 rings of given size next to each other, see the insets. In the honeycomb case (blue), the (6,6,6) triplet is by far the most common, as we would expect for this lattice built of hexagons. Other significant fractions include (5,6,7), a typical defect element (grain boundaries [1]), (5,6,6), and (6,6,7). In the amorphous case (yellow), the triplet probability is much more broadly distributed. However, it is clear that some combinations are more common than others; for instance, the (5,6,7) triplet is roughly 2

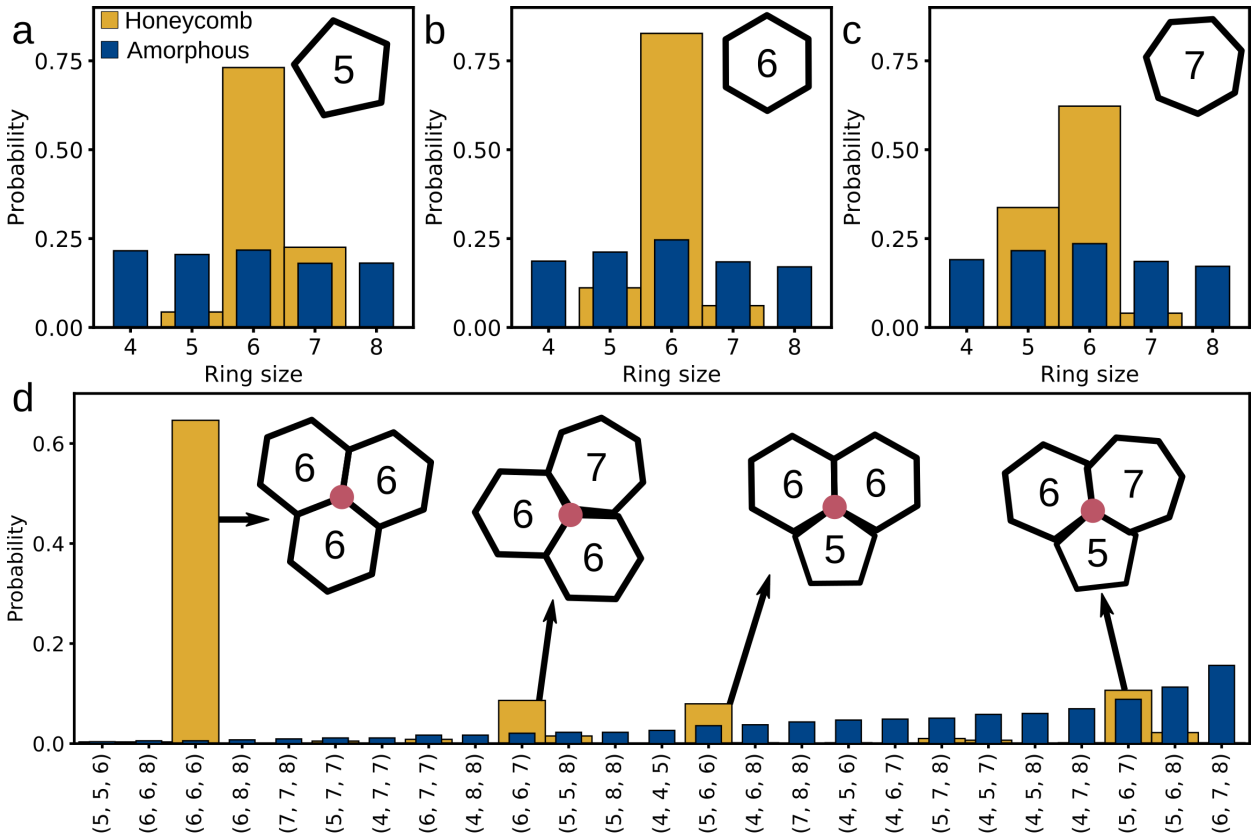

Supplementary Figure 3. **Characterization of particle neighbourhoods from adjacent rings.** Probability of finding an n-membered ring neighbouring a 5-membered ring (a), neighbouring a 6-membered ring (b), and neighbouring a 7-membered ring (c). (d) Probability of encountering ring triplet combinations in the honeycomb and amorphous phase. In all panels, honeycomb is indicated in yellow, and amorphous network in blue. We use the same experimental data that was used in Fig. 2a of the main text.

times more common than the (5,6,6) triplet. This indicates that the amorphous phase is still somewhat ordered over 'medium' distances. This matches similar observations in other trivalent amorphous networks, like amorphous silica [1].

SUPPLEMENTARY NOTE 4: ORDER PARAMETERS

In this work, we define two order parameters, $\langle N_{\mathrm{nb}} \rangle$ and R, to identify the transition between phases. The average number of neighbours $\langle N_{\mathrm{nb}} \rangle$ is a simple measure that can be

used to distinguish fluid from honeycomb. Particles in a honeycomb lattice are characterized by having exactly 3 neighbouring particles, while particles in the fluid phase have no bonds (or rather, only bonds with a short lifetime). Therefore, a transition from almost no to several neighbours signals the transition from fluid to fluid/honeycomb, as seen in Figure 3a and 3d of the main text. However, $\langle N_{\mathrm{nb}} \rangle$ is less suitable for characterization of the transition or coexistence between condensed phases.

For those, we take the peak ratio R, which we determine from the characteristic height of the $g(r)$ peaks at 1.74σ and 2.00σ, and is able to distinguish structures from their second-nearest neighbor environment. When our system transitions from an open structure (like a honeycomb lattice or amorphous network) to a closed lattice (the triangular lattice), the systems' radial distribution function undergoes a small but significant change, as illustrated in Figure 2b of the main text. The most obvious change occurs at the 2σ peak, which is significantly larger in the triangular phase due to the particle occupying each hexagonal ring.

In the honeycomb lattice there are six neighbours in the second coordination shell and three neighbours in the third coordination shell, while in the triangular phase there are six neighbours in each of these two coordination layers (see Supplementary note 2). Therefore, we can use the ratio between the varying third shell peak at 2σ and the unchanging second shell peak at 1.74σ to follow the transition from open to closed structure; we define the ratio between the two peaks as:

$$R = \frac{\int_{1.9\sigma}^{2.1\sigma} g(r)\ \mathrm{d}r}{\int_{1.6\sigma}^{1.9\sigma} g(r)\ \mathrm{d}r}. \tag{1}$$

In a perfect honeycomb lattice, $R = 0.5$, since the second coordination shell has 3 particles, while the third has 6. In practice, values in the order of $R = 0.75$ are observed due to defects. In a perfect closed triangular lattice, $R = 1$, since the second and third coordination shell both have 6 particles. A value closer to $R = 1.25$ is typically observed in our experiments due to overlapping of the peaks for the second and third shell. Finally, in the disordered fluid phase, there are no specific peaks at these typical distances, leading to a value of $R = 1$.

This feature can also be described by a more conventional order parameter like ψ_6 [2, 3]. However, it turns out that in practice, parameter R gives a better contrast between the two phases in our system.

We use this ratio R as order parameter to determine coexistence points between two phases in Figure 3 of the main text.

SUPPLEMENTARY NOTE 5: SIMULATION DETAILS

The potential

The interaction between particles in the simulations is described by a generalized Lennard-Jones (LJ) repulsive core and an attractive tail modulated by an angular dependent function [4, 5]:

$$V_{ij}(\mathbf{r}_{ij}, \mathbf{\Omega}_i, \mathbf{\Omega}_j) = \begin{cases} V'_{\mathrm{LJ}}(r_{ij}) & : r_{ij} < \sigma'_{\mathrm{LJ}} \\ V'_{\mathrm{LJ}}(r_{ij}) V_{\mathrm{ang}}(\hat{\mathbf{r}}_{ij}, \mathbf{\Omega}_i, \mathbf{\Omega}_j) & : r_{ij} \geq \sigma'_{\mathrm{LJ}} \end{cases}, \tag{2}$$

where $\mathbf{r}_{ij}$ is the inter-particle vector, α and β are patches on particles i and j, respectively, $\mathbf{\Omega}_i$ is the orientation of particle i, $V'_{\mathrm{LJ}}(r)$ is a cut-and-shifted $m-n$ LJ potential and σ'_{LJ} corresponds to the distance at which V'_{LJ} passes through zero:

$$V'_{\mathrm{LJ}}(r_{ij}) = \frac{n}{n-m}\left(\frac{n}{m}\right)^{\frac{m}{n-m}} \epsilon_{LJ}\left(\left(\frac{\sigma_{LJ}}{r_{ij}}\right)^n - \left(\frac{\sigma_{LJ}}{r_{ij}}\right)^m\right) \tag{3}$$

The exponents of the generalized-LJ model are assigned large values, in particular 200-100, to obtain a short-ranged model mimicking that found in experiments of colloidal particles. The cut-off distance is set to $r_{\mathrm{cut}} = 1.10\,\sigma_{\mathrm{LJ}}$, at which the energy is rather small (-0.0029ϵ).

The angular modulation term V_{ang} is a measure of how directly the patches α and β point at each other, and is given by

$$V_{\mathrm{ang}}(\hat{\mathbf{r}}_{ij}, \mathbf{\Omega}_i, \mathbf{\Omega}_j) = \exp\left(-\frac{\theta^2_{\alpha ij}}{2\sigma^2_{\mathrm{ang}}}\right)\exp\left(-\frac{\theta^2_{\beta ji}}{2\sigma^2_{\mathrm{ang}}}\right), \tag{4}$$

$\theta_{\alpha ij}$ is the angle between the patch vector $\hat{\mathbf{P}}^{\alpha}_i$, representing the patch α, and $\hat{\mathbf{r}}_{ij}$. Each particle has four patches distributed tetrahedrally on the particle surface. σ_{ang} is a measure of the angular width of the patch. In this study, the angular width is set to σ_{ang}=0.52 radians, based on a combination between direct experimental observation of the bond angle (see Supplementary note 7), and matching of the simulated ring counts and phase diagram with experiments.

The patches interact also with the bottom surface through the same interaction potential (Eq. 3). The difference is that now the distance between the particle and the surface is given by the z-coordinate of the particle position vector, and the angular term depends only on the Gaussian of the angle of the interacting patch with the normal to the surface.

The interaction strength between a particle and the bottom surface is set to four times the interaction between two particles. We use $\sigma_{\rm LJ}$ as the unit of length, and the LJ well depth $\varepsilon_{\rm LJ}$ as the unit of energy. Temperatures are given in reduced form:

$$T^* = k_B T/\varepsilon_{\rm LJ}. \tag{5}$$

Besides these interactions, to mimic the experimental conditions, particles were also subject to a gravitational potential:

$$u_{\rm grav}(z) = \frac{z}{l_{\rm grav}} k_{\rm B} T \tag{6}$$

where $l_{\rm grav}$ is the gravitational length, whose value was estimated from the relation $l_{\rm grav} = k_{\rm B}T/\Delta\rho V_{\rm c} g$, where $\Delta\rho$ is the density difference between the colloids and the solvent, $V_{\rm c}$ is the volume of the colloidal particles and g is the gravitational constant. Here, we took $l_{\rm grav} = 0.5865\sigma_{\rm LJ}$. Note, however, that the effect of this term once the particles are deposited on the surface is small, because the strength of the wall with the particles' patches is stronger.

Simulations

We use Metropolis Monte Carlo to simulate the patchy-particle systems in the canonical ensemble (NVT). The simulations are performed in an orthorhombic box with $N = 900$ colloidal particles. Periodic boundary conditions are applied along the x and y axes. Several lengths of the simulation box along the x and y, L_x and L_y, are used to cover surface packing fractions, $\eta = N\pi/L_x/L_y/4$, between 0.001 and 0.85. In order to minimize the incommensurability of the assembled honeycomb and triangular lattices with the simulation box, we set $L_x = 2/\sqrt{3}L_y$. L_z is initially set to $L_z = 100\sigma_{\rm LJ}$. Particles are initially distributed randomly in the simulation box. The system is then allowed to evolve until all the particles sediment and bind to the bottom surface. Using this state as the initial configuration, simulations are then performed at different temperatures. To improve the sampling, besides normal MC moves, aggregation volume moves (AVB) [6] are also performed. The acceptance probability of the MC moves is set to 50-70%. Typically, the MC simulations consist of 100 million MC cycles, where one cycle is defined as N attempts to translate or to rotate a particle. At the lower temperatures, simulations need to be twice or three times longer to get well converged results.

SUPPLEMENTARY NOTE 6: COMPARING SIMULATIONS AND EXPERIMENTS

While the reduced temperature T^* sets the interaction strength between particles in simulations (see Supplementary Methods below), the distance to the critical temperature $\Delta T = T - T_c$ sets the interaction strength in experiments. Unfortunately, conversion between these two parameter is non-trivial, which hinders direct comparison of simulations and experimental results. To nevertheless calibrate the simulations to the experimental system to allow comparison of their behavior, we plot the inter-patch potentials in simulations, together with the best estimation of the experimental ones in Supplementary Figure 4. The simulated potentials result from the Lennard-Jones potential of eq. 3, while the experimental critical Casimir potential is estimated based on the critical Casimir potential model presented in [7], and calibrated for our patchy particles in [8]. For the purpose of the current paper, we select values of ΔT and T^* that result in approximately the same potentials, so we can most easily relate them. Figure 4b of the main text lends credence to this approach: the average number of neighbours $\langle N_{\mathrm{nb}} \rangle$ as a function of area coverage η in experiments and simulations almost perfectly overlap for $\Delta T = 0.42°C$ and $T^* = 0.2$, in agreement with their matching potentials in Supplementary Figure 4.

SUPPLEMENTARY NOTE 7: BENDING ANGLE RIGIDITY

The bond-bending potential is hard to estimate from the geometry of individual particles, but can be determined from experimental measurements. By following three bonded particles and tracking the fluctuations of their bond angles, we can determine the bending energy by assuming a Boltzmann distribution. The resulting bending energy as a function of angle, determined from the probability distribution of bond angles, is shown in Supplementary Figure 5. The shape of this potential can be fitted with a parabola assuming a harmonic potential (Hooke's law). This leads to a bending stiffness with a force constant of $39.4 k_{\mathrm{B}} T / rad^2$.

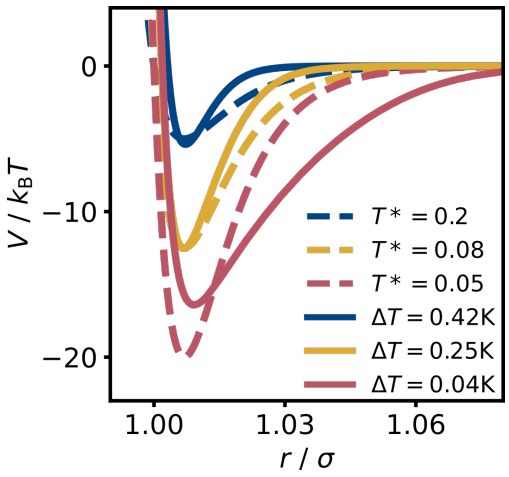

Supplementary Figure 4. **Inter-particle potential in simulations and experiments.** The inter-particle potential V in units $k_\mathrm{B}T$ as a function of distance between particles centres r in units diameter. We compare the potential in simulations at three reduced temperatures (dashed lines) with estimated critical Casimir potentials in experiment (solid lines). Although the potentials do not match perfectly, we can estimate that comparable behaviour is expected at potentials with the same colour.

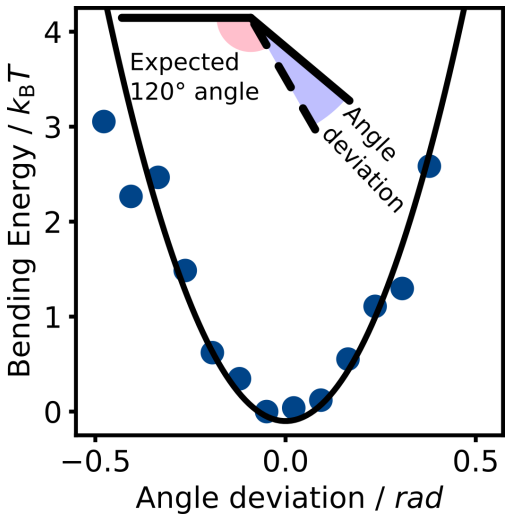

Supplementary Figure 5. **Bond energies of Patchy Particles** The experimentally determined bending potential (blue circles) between 3 patchy particles at $\Delta T = 0.05°C$. The black solid line is a simple Hookean fit, which assumes a simple spring: $U_\mathrm{bend} = \frac{1}{2}k_\mathrm{bend}\theta^2$, with force constant $k_\mathrm{bend} = 39.4k_\mathrm{B}T/\mathrm{rad}^2$.

SUPPLEMENTARY METHODS

Supplementary Method 1: Sample Preparation and Glass Silanization

The patchy particles are stored dispersed in water with a small amount of F108 copolymer as stabilizer ($< 0.05\%$wt). To prepare a sample stock, particles are transferred to the binary solvent by washing them at least 4 times in the desired binary mixture. To prepare a sample for microscopy, a small amount of the sample is injected into a glass capillary (Vitrotubes, Rectangle Boro Tubing 0.20×2.00mm) and sealed with teflon grease (Krytox GPL-205).

The glass capillaries are silanized, making them hydrophobic. The hydrophobic treatment for capillaries is a simple gas silanization reaction, briefly: The capillaries are cleaned thoroughly using a piranha treatment, or alternatively using Hellmanex III and plasma treatment. Capillaries are then placed in a vacuum desiccator together with approx. 1 ml of hexamethyldisilazane (HMDS) ($\geq 99.0\%$, Sigma-Aldrich). Pressure is lowered to below 200 mbar using a pump, and kept low for at least 2 hours. The capillaries are then baked in an oven at 120°C for circa 1 hour [9–11].

Supplementary Method 2: Observation by confocal microscopy

Particles are left to sediment to the bottom of the sample at room temperature before measurements. We tilt the sample slightly during sedimentation, so a small density gradient is present in the sample. We then heat the sample to $33.45°C$ ($\Delta T \approx 0.65°C$), which causes one of the particle patches to attach to the sample wall. For heating, we use a well-controlled temperature stage in combination with an objective heating element, capable of reaching a relative accuracy of $0.01°C$.

In an experiment, we typically heat a sample to a certain ΔT below the phase separation temperature of the lutidine-water mixture, inducing critical Casimir attraction between patches. The structures then grow by two-dimensional diffusion in the plane. No mixing is necessary. After several hours of equilibration, we investigate the structures using a 100x oil-immersion objective.

We image the assembled structures using confocal microscope image stacks, sometimes alternating with bright field images. Particle centres are determined with techniques described in SI [12].

The phase diagram in Fig. 4a and lines in Fig. 3 of the main text are generated from two individual samples. However, quantitatively similar results are obtained in several other samples, with only slight differences in phase transition temperatures. This difference results mostly from minute differences in the water-lutidine composition of the solvent, which can strongly influence interaction strength and its change as a function of temperature [13]. We therefore focus on these two representative samples to prevent individual variation between samples, which would blur phase transitions and order parameters.

Supplementary Method 3: Tracking Patchy Particles

We analyse confocal images using particle tracking software (Trackpy [12]) to determine the centre of each fluorescent patch. In our experiments, the particles are all at the same height, having one patch bound to the capillary surface and the other three available for bonding. In Supplementary Figure 6a, we show a typical confocal microscope image of the tetrapatch particles bonded in a 6-membered ring (hexagon), and in Supplementary Figure 6b we show a schematic reconstruction with the particle patches indicated in orange. In this reconstruction, each particle has one patch in the centre of the particle, and 3 patches at the boundary. To find particle positions, we perform the following actions:

1. Determine the location of each individual fluorescent patch using Trackpy in 2 dimensions (the z-axis is fixed in this system, so determination is possible, but superfluous).

2. Find all other patches within approximately one particle diameter using a kd-tree (implemented in SciPy), and connect those into a network.

3. In the resulting network (Supplementary Figure 6c), we find all triangles.

4. For each triangle, we determine the mean edge length and the variation of this value. We only select triangles where the mean edge length d is close to the expected value based on the radius r ($d = \frac{4}{\sqrt{3}}r$), and where the edge length variation is small, see

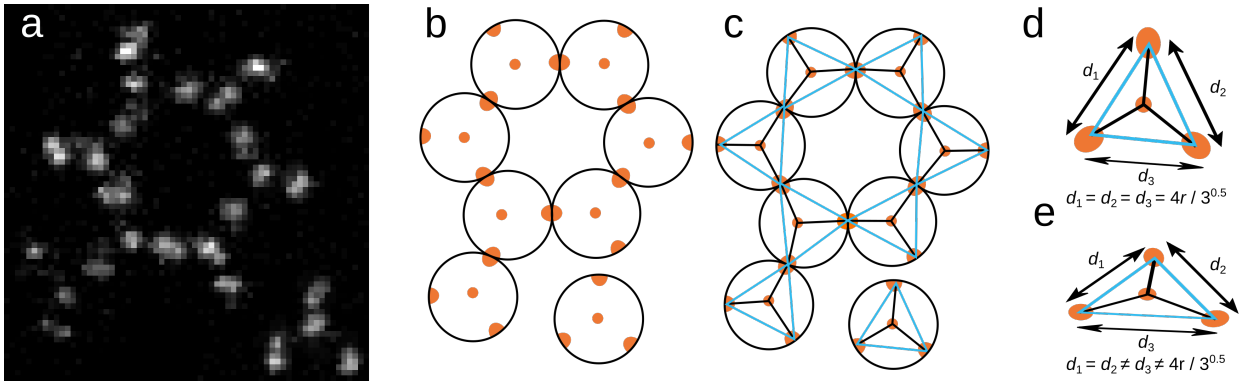

Supplementary Figure 6. **Tracking and reconstruction procedure.** (a) Representative z-projected confocal microscope image of tetrapatch particles bonded into a hexagon. (b) Schematic reconstruction of the particle arrangement corresponding to (a). Particles have a black outline, patches are shown in orange. In (a), the central patch is slightly out of focus, and is thus less bright. (c) Corresponding network formed by connecting all patches within a particle radius of each other. Regular triangles shown in cyan demarcate the connected outer patches belonging to one particle. (d) A group of 4 patches belonging to the same particle, forming a regular tetrahedron, which has edges with the expected length. All edges have equal lengths within particle dispersity and tracking error bars. (e) A group of 4 patches not belonging to the same particle, forming an irregular tetrahedron, where not all edges have the same length, and not all edges have the expected length.

Supplementary Figure 6d and e. This means we effectively select the blue triangles in Supplementary Figure 6c.

We are left with a triangle with 3 vertices corresponding to the outer patches. In the centre of the triangle is the patch bound to the surface. Based on this procedure, bonds between particles are then easily determined by checking which patches are shared between particles.

---

[1] Christin Büchner, Liwei Liu, Stefanie Stuckenholz, Kristen M. Burson, Leonid Lichtenstein, Markus Heyde, Hong-Jun Gao, and Hans-Joachim Freund. Building block analysis of 2D amorphous networks reveals medium range correlation. *Journal of Non-Crystalline Solids*,

435:40–47, March 2016.

[2] Paul J. Steinhardt, David R. Nelson, and Marco Ronchetti. Bond-orientational order in liquids and glasses. *Physical Review B*, 28(2):784–805, July 1983.

[3] Qian Chen, Sung Chul Bae, and Steve Granick. Directed self-assembly of a colloidal kagome lattice. *Nature*, 469(7330):381–384, January 2011.

[4] J. P. K. Doye, A. A. Louis, I.-C. Lin, L. R. Allen, E. G. Noya, A. W. Wilber, H. C. Kok, and R. Lyus. Controlling crystallization and its absence: Proteins, colloids and patchy models. *Physical Chemistry Chemical Physics*, 9:2197–2205, 2007.

[5] E. G. Noya, C. Vega, J. P. K. Doye, and A. A. Louis. The stability of a crystal with diamond structure for patchy particles with tetrahedral symmetry. *Journal of Chemical Physics*, 132:234511, 2010.

[6] B. Chen and J. I. Siepmann. Optimized monte carlo data analysis. *Journal of Physical Chemistry B*, 105:11275, 2001.

[7] S. G. Stuij, M. Labbé-Laurent, T. E. Kodger, A. Maciołek, and P. Schall. Critical Casimir interactions between colloids around the critical point of binary solvents. *Soft Matter*, 13(31):5233–5249, 2017.

[8] H. J. Jonas, S. G. Stuij, P. Schall, and P. G. Bolhuis. A temperature-dependent critical Casimir patchy particle model benchmarked onto experiment. *The Journal of Chemical Physics*, 155(3):034902, July 2021.

[9] Jay W. Grate, Marvin G. Warner, Jonathan W. Pittman, Karl J. Dehoff, Thomas W. Wietsma, Changyong Zhang, and Mart Oostrom. Silane modification of glass and silica surfaces to obtain equally oil-wet surfaces in glass-covered silicon micromodel applications. *Water Resources Research*, 49(8):4724–4729, 2013.

[10] Annina M. Steinbach, Tanja Sandner, Boris Mizaikoff, and Steffen Strehle. Gas phase silanization for silicon nanowire sensors and other lab-on-a-chip systems. *physica status solidi c*, 13(4):135–141, 2016.

[11] Walid-Madhat Munief, Florian Heib, Felix Hempel, Xiaoling Lu, Miriam Schwartz, Vivek Pachauri, Rolf Hempelmann, Michael Schmitt, and Sven Ingebrandt. Silane Deposition via Gas-Phase Evaporation and High-Resolution Surface Characterization of the Ultrathin Siloxane Coatings. *Langmuir*, 34(35):10217–10229, September 2018.

[12] Daniel B. Allan, Thomas Caswell, Nathan C. Keim, Casper M. van der Wel, and Ruben W.

Verweij. Soft-matter/trackpy: Trackpy v0.5.0. Zenodo, April 2021.

[13] C Hertlein, L Helden, A Gambassi, S Dietrich, and C Bechinger. Direct measurement of critical Casimir forces. *Nature*, 451(January), 2008.